Nanoscale

Accepted Manuscript

This article can be cited before page numbers have been issued, to do this please use: T. Blondy, J. Poly, C. Linot, J. Boucard, E. Allard-Vannier, S. Nedellec, P. Hulin, C. Henoumont, L. Larbanoix, R. N. Muller, S. Laurent, E. Ishow and C. Blanquart, *Nanoscale*, 2022, DOI: 10.1039/D1NR06769A.

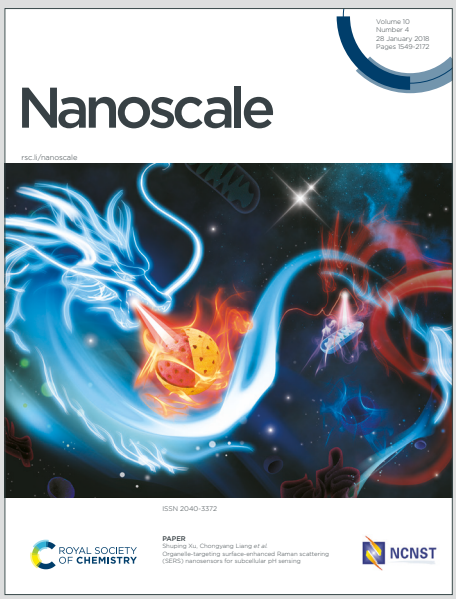

ROYAL SOCIETY OF CHEMISTRY

rsc.li/nanoscale

Impact of RAFT Chain Transfer Agents on the Polymeric Shell Density of Magneto-Fluorescent Nanoparticles and Their Cellular Uptake

Received 00th January 20xx,
Accepted 00th January 20xx

DOI: 10.1039/x0xx00000x

Thibaut Blondy,[a] Julien Poly,[b] Camille Linot,[a] Joanna Boucard,[a,c] Emilie Allard-Vannier,[d] Steven Nedellec,[e] Phillipe Hulin,[e] Céline Hénoumont,[f] Lionel Larbanoix,[g] Robert N. Muller,[f] Sophie Laurent,[f,g] Eléna Ishow*,[c] and Christophe Blanquart*,[a]

The impact of nanoparticle surface chemistry on cell interactions and especially cell uptake has become evident over the last years in nanomedicine. Since PEG polymers have proved to be ideal tools to attain stealthiness and favor escape from the *in vivo* mononuclear phagocytotic system, accurate control of their geometry is of primary importance and can be achieved through reversible addition-fragmentation transfer (RAFT) polymerization. In this study, we demonstrate that the residual groups of the chain transfer agents (CTA) introduced in the main chain exert significant impact on the cellular internalization of functionalized nanoparticles. High-resolution magic angle spinning ^{1}H NMR spectroscopy and fluorescence spectroscopy permitted by the magneto-fluorescent properties of the nanoassemblies (NAs) reveal compaction of the PEG comb-like shell incorporating CTAs with a long alkyl chain, without changing the overall surface potential. As a consequence of the capability of alkyl units to self-assemble at the NA surface while contributing to hardly more than 0.5 % to the total polyelectrolyte weight, denser PEGylated NAs show notably less internalization in all cells of the tumor microenvironment (tumor cells, macrophages and healthy cells). Interestingly, such differentiated uptake is also observed between pro-inflammatory M1-like and immunosuppressive M2-like macrophages, the latter phagocytizing more efficiently NAs coated with a less compact PEGylated shell. By contrast, the NA diffusion inside multicellular spheroids, used to mimic solid tumors, appears independent on the NA coating. These results provide a novel effort-saving approach where the sole variation of the chemical nature of CTAs in RAFT PEGylated polymers strikingly modulate the cell uptake of nanoparticles upon organization of their surface coating, and open the pathway toward selective addressing of macrophage populations for cancer immunotherapy.

1. Introduction

The production of nanometer-sized multifunctional nanomaterials has stimulated tremendous attention for their ability to provide reliable diagnostics upon crossed bioimaging techniques, reduce treatment side-effects upon selective targeting, and combine chemotherapeutic agents with tracers to finely track or stimulate drug delivery.[1-4] In order to face the complexity of biological media, various synthesis guidelines, based on thorough physicochemical investigations, have emerged regarding the nano-object size,[5-7] shape,[8-10] surface functionalization,[11] elasticity[12-13] and surface charge,[14] known to rule the nanoparticle-cell interactions. In this respect, the surface charge of nanoparticles was found to considerably impact their cell entry capability and *in vivo* fate due to activation of the mononuclear phagocytic system, conducting to fast clearance from the bloodstream.[15] For this reason, neutral coatings provided by hydrophilic poly(ethylene glycol) (PEG) chains,[16-17] as well as zwitterionic ligands,[7,18-20] have been developed and are nowadays indisputably recognized to provide long circulation time by repelling from their surface opsonins, facilitating phagocytosis for fast nanoparticle clearance. Numerous investigations have thus been carried out to rationalize the effect of the PEG chain length and morphology on the shell compacity to cite only a few.[17,21-23] Indeed, the latter regulates the adhesion of proteins from serum and blood,[24-27] controls the rate of internalization in cancer cells,[28-30] and impacts the contrast efficiency in magnetic resonance imaging by influencing the diffusion and retention time of water molecules near the paramagnetic or superparamagnetic nanomaterials.[31-33] In this context, controlling the polymer structure has become of utmost importance, which can be achieved by adopting controlled radical polymerization reactions. Among them, the reversible addition-fragmentation transfer (RAFT) process has appeared particularly attractive for its easy access to amphiphilic polymers using water-soluble macromonomers with a high structural control.[34] RAFT polymerization usually implies vinylic monomers as well as a chain transfer agent (CTA) whose chemical nature is chosen as a function of the reaction solvent, the monomer reactivity and the possibility of cleavage for ulterior (bio)functionalization (Fig. 1).[35] A large panel of RAFT CTAs is thus available and all generic structures incorporate a labile R group contributing to reinitiating the chain growth and a fixed Z-activating group.[36] Both groups are located at the terminal ends of the polymer chain, namely R at the α position after a multiple sequence of addition-fragmentation steps, and Z at the ω position through a fixed C-C bond. Surprisingly, the potential influence of their chemical nature on cell interactions has aroused very little consideration. This is in strong contrast with the specific care taken to vary the charge of the monomeric units by incorporating anionic

a, Nantes Université, Univ Angers, INSERM, CNRS, CRCI2NA, F-44000 Nantes, France.
b, IS2M-UMR CNRS 7361, Université de Haute Alsace, 15 rue Jean Starcky, 68057 Mulhouse, France.
c, Nantes Université, CNRS, CEISAM, UMR 6230, F-44000 Nantes, France.
d, EA 6295 'Nanomédicaments et Nanosondes', Université de Tours, Tours, F-37200, France.
e, Nantes Université, INSERM, UMS 016, CNRS, UMS 3556, F-44000 Nantes, France.
f, Department of General, Organic, and Biomedical Chemistry, NMR and Molecular Imaging Laboratory, University of Mons-Hainaut, B-7000 Mons, Belgium.
g, Center for Microscopy and Molecular Imaging, 8 rue Adrienne Bolland à Gosselies, 6041 Gosselies, Belgium.
† Footnotes relating to the title and/or authors should appear here.
Electronic Supplementary Information (ESI) available: [details of any supplementary information available should be included here]. See DOI: 10.1039/x0xx00000x

or cationic units, which induces the formation of distinct protein coronae due to the differentiated adsorption of proteins present in the plasma or cell cytofluid.[37-38] And yet, a recent report showed distinct behaviors in terms of MRI contrast and cell uptake for two series of anionic magneto-fluorescent superparticles, displaying both a comb-like PEGylated outer shell but differing by their synthesis process (classical versus RAFT polymerization) and the presence of a Z group comprising a long alkyl chain.[39] To go a step further, we want to show herein that fine structural tuning of the hydrophobic Z group can induce noteworthy differences in the dynamics of cellular internalization not only by cancer cells but also by cells from the tumor microenvironment including macrophages and primary healthy cells, which represents a high stake due to the considerable regulation role played by macrophages on cancer development.[40] With this aim in mind, two models of thoracic cancers were employed comprising malignant pleural mesothelioma (MPM), a particularly aggressive cancer related to asbestos exposure facing terrible therapeutic standoff, and lung adenocarcinoma, a leading cause of death worldwide.[41-42] Structural investigations of the polymer coating permitted by ^{1}H NMR and high-resolution magic angle spinning (HR-MAS) protocols shine light on the spatial organization in water of the PEGylated polyelectrolytes at the nano-object surface. Besides quantitative assessment of the coating density, such studies will help to establish tight relationships between the microscopic arrangement of the polymers at the nanoparticle surface, and the macroscopic biological behaviors of the nanoparticles, by taking advantage of their fluorescent and magnetic properties. We will especially study the differentiated internalization efficiency of nanoparticles in malignant cells, grown as monolayers and as 3D multicellular tumor spheroids mimicking solid tumor, and their long-term fate. Finally, with the prospect of systemic injection for cancer treatment, a commonly applied protocol in clinical transfer, we push forward the nanoparticle internalization evaluation in monocytes and lymphocytes, largely present in blood, and in macrophages and primary mesothelial cells, present in the tumor microenvironment. All these unified studies should open attractive pathways toward cancer treatments based on cleverly designed drug nanocarriers with discriminating capabilities of cell internalization.

2. Results and discussion

2.1 Modular synthesis of magneto-fluorescent nanoassemblies with distinct RAFT polyelectrolyte coatings

Magneto-fluorescent nano-architectures[43-46] have showed to be particularly attractive to evaluate or manipulate[47-48] the biological interactions of nano-objects with low-radiation risks and high-resolution imaging tools like fluorescence microscopy imaging and magnetic resonance imaging (MRI).[49-52] Their bimodality enables easily implementable cellular and *in vivo* investigations, facilitating the transfer from bench to animal studies. In this context, for several years, we have developed core-shell nanoassemblies (NAs) that advantageously comprise a bright organic core made of self-assembled hydrophobic fluorophores, surrounded by a compact magnetic shell of superparamagnetic iron oxide nanoparticles (SPIONs).[44,53] Simultaneously, the high magnetic payload creates large surface magnetic inhomogeneity, generating a tenfold increase in MRI contrast compared to those recorded with single isolated magnetic nanoparticles.[54] The modular and straightforward synthesis of these bimodal nanoassemblies is based first on the flash nanoprecipitation of fluorescent organic nanoparticles (FONs) in an acidic dispersion of SPIONs that spontaneously cover the FON surface thanks to the chelating phosphonic moieties of the precipitated fluorophores endowed with high affinity toward iron oxides.[55-57] In a second step, the addition of carboxylate polyelectrolytes anchoring the outer magnetic shell affords NAs with large colloidal stability in water and saline media, insignificant toxicity effects, as well as access to further bioconjugation when required.[53] Thus, the "onion-like" NA construction allows us to easily vary the nature of the added polyelectrolytes, and explore the incidence of their chemical structure on cell uptake efficiency and kinetics over a large panel of cells that intervene in the blood (monocytes and lymphocytes) as well as in the tumor microenvironment (tumor cells, macrophages and primary healthy cells). In order to probe the biological effects caused by fine structural changes at the nanoparticle interface, two anionic PEGylated polyelectrolytes **P2** and **P3** were synthesized by resorting to RAFT controlled radical polymerization process, highly praised for the production of biocompatible polymers with narrow size distributions (Table 1, Fig.1).

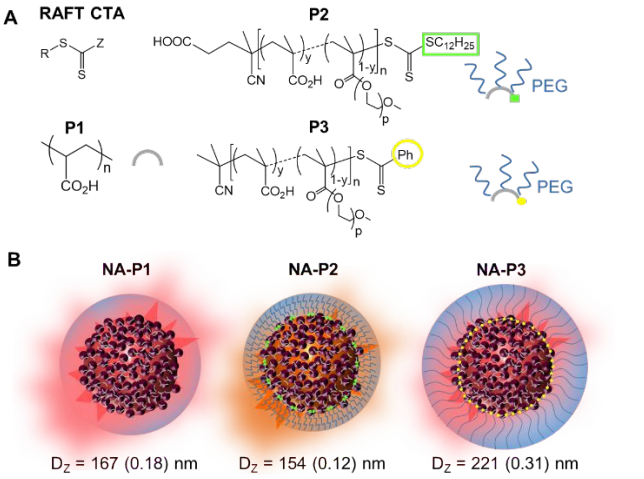

Fig. 1 A) Generic structure of RAFT charge transfer agent with R and Z designating the labile and activating groups, respectively, and structure of the polyelectrolytes **P1** and **P2-P3** serving as external coating of the magneto-fluorescent nanoassemblies (NAs) through their carboxylic acid units existing as carboxylate in water. B) Schematic structures of the nanoassemblies **NA-Px** (x = 1, 2, 3) and hydrodynamic diameter D_Z (PDI) on the basis of ^{1}H HR-MAS spectroscopic, DLS and photophysical analyses (for sake of clarity, the PEG chains are not represented at the front of the nanoassemblies; the extension of the solvation shell provided by DLS measurements is depicted as a blue disk).

The length of the targeted poly(methacrylic acid) (PMAA) main chain was chosen close to that of the polyacrylate **P1**, serving as a relevant biocompatible model to evaluate the stealthiness conferred by the presence of comb-like PEG chains on **P2** and **P3** (see Supporting Information – part 3). Their PEGylation density was kept identical. Hence the **P2** and **P3** structures only differ in their terminal units as a result of the incorporation of distinct RAFT transfer agents, namely a trithiocarbonate comprising a dodecyl chain, and a dithiobenzoate comprising a phenyl unit respectively. The choice for both these RAFT CTAs was motivated by their purely hydrophobic character and their

similar reactivity toward the water-soluble MAA monomer and MAPEG macromonomer. The presence of the trithiocarbonate and dithiobenzoate Z groups was confirmed by UV-vis absorption spectroscopy in water, evidencing their typical ππ* transitions around 300 and much weaker nπ* transitions around 450-500 nm, the latter being responsible for the pale yellow and pink colors noticed for **P2** and **P3** respectively (Fig. S1).

Table 1 Structural parameters of the polyelectrolytes Px (x = 1, 2, 3) coating the surface of the magneto-fluorescent nanoassemblies NA-Px.

Polyelectrolyte	M_n (g.mol^{-1})[a]	$Đ$[a]	n[b]	p[c]	y[d]
P1	1.8×10^3	n.a.	24	0	1
P2	3.99×10^4	1.30	30	43	0.8
P3	2.87×10^4	1.20	25	43	0.8

[a] Determined by SEC analyses using DMF as the solvent; Đ designates the polymer dispersity determined by SEC. [b] n = theoretical degree of polymerization, with n = ($[MMA]_0$ + $[MAPEG]_0$) / $[CTA]_0$. [c] p = degree of polymerization calculated from the molecular weight of the commercially available PEG macromonomers. [d] y = molar fraction of MMA and MAPEG monomers used in the synthesis and theoretical molar fraction for quantitative conversion, with y = $[MMA]_0$ / ($[MMA]_0$ + $[MAPEG]_0$).

Here, the formation of RAFT homopolymers can be ruled out. On the one hand, if poly(methacrylic acid) were formed, its low average molecular weight would be incompatible with SEC characterizations. On the other hand, the formation of pegylated poly(methacrylate) could not lead to complexation of the magneto-fluorescent NAs due to the absence of chelating carboxylate moieties.

All resulting **NA-Px** (x = 1, 2, 3) showed a raspberry-like architecture with a hydrodynamic diameter D_Z (also called intensity Z-averaged hydrodynamic diameter) around 150-230 nm as measured by dynamic light scattering. Due to the loss of the hydration sphere under vacuum, smaller dry diameters D_{TEM} around 70-80 nm are systematically measured by transmission electron microscopy (TEM) (Fig. 2, Table 2).[35] The lower negative ζ surface potentials measured at -12 mV for **NA-P2** and **NA-P3** compared to -44 mV for **NA-P1** stems from the lower amount of methacrylate units on the main chain due to the incorporation of PEGylated macromonomers in a 20 % ratio with regard to the methacrylate monomers. As reported later, such values do not prevent the nanoassemblies from being internalized in cells, although a longer time (6 to 24 h) was required than that usually reported (~1 h) for positively charged nanoparticles. This also ensures low cytotoxicity effects due to weak electrostatic destabilization of the cytoplasmic membrane that occurs in the presence of a large flow of positively charged nano-objects.[58] For all **NA-Px** assemblies, such values as well as the PEG chains ensured colloidal stability in various media like Millipore water, saline solutions of various ionic strength (150 and 300 mmol.L^{-1}), and PBS buffer (Fig. S2, Table S1). Interestingly, the fluorescence signal underwent a pronounced hypsochromic shift from 614 nm for **NA-P1**, to 603 nm for **NA-P3** and eventually 591 nm for **NA-P2** (Table 2, Fig. 3). Since the larger structural discrepancy between **P2** and **P3** relies on the chemical nature of the Z activating group of the RAFT CTAs, we suspect that the latter may be responsible for the change in the NA absorption maximum. From previous studies, we know that a hypsochromic shift features less polar surroundings.[59] This suggest an orientation of the alkyl terminal ends in the **P2** PMAA main chain toward the nanoassembly surface. Therefore, water molecules would be repelled and form a remote hydration shell, as evoked earlier to explain relaxometry differences.[39] Unlike phenyl groups present in **P3**, dodecyl chains are known for their propensity to provide stiff self-assembled layers through London interactions.[60] It seems reasonable to consider that such self-organization of the dodecyl chains in **P2** could impact the PEG chain distribution in water. Interestingly, the consideration of polydispersity index (PDI) shows a slightly higher value (0.23) for **NA-P3** whereas the PDI values are very similar in the dry state (0.15-0.22) (Table 2). This lets us suggest that **NA-P3** coating is more mobile, less organized, and consequently less dense, thereby enabling larger dynamics of the solvent shell.

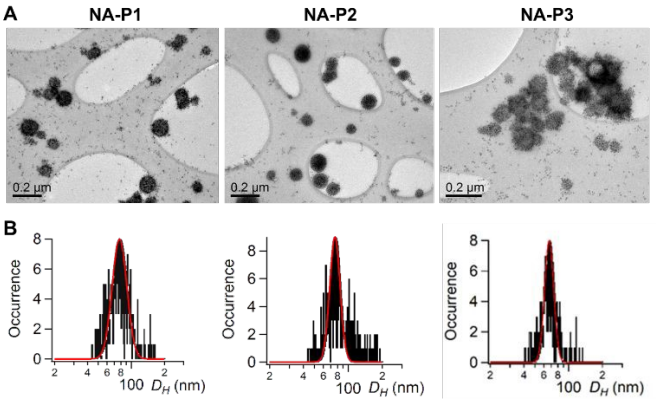

Fig. 2 A) TEM imaging of **NA-P1**, **NA-P2** and **NA-P3** dispersions deposited on holey carbon-coated copper grids (80 keV imaging voltage). B) Size distribution from counting 200 **NA-Px** (x = 1,2,3).

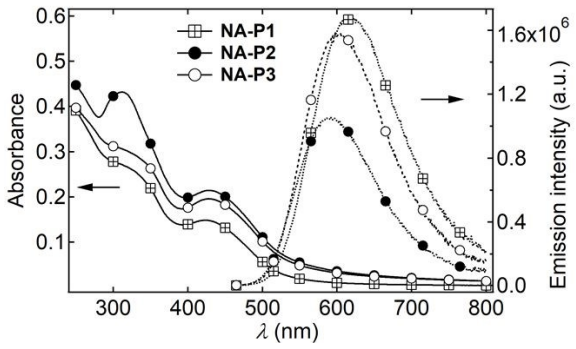

Fig. 3 Absorption spectra continuous line) and emission spectra (dotted line; λ_{exc} = 450 nm) of **NA-P1**, **NA-P2** and **NA-P3** dispersions in Millipore water. All stock solutions were diluted by a factor of ten for the spectroscopic measurements.

To test this hypothesis and gain insight in the structuration of the NA outer coating in water, nuclear proton relaxation of the polyelectrolyte would represent an ideal tool. However, the presence of superparamagnetic species like SPIONs causes an additional magnetic field, which is highly detrimental for high-quality NMR spectra and prohibits classical NMR investigations on organic ligands grafted at the SPION surface.

2.2 Microscopic studies of the polyelectrolyte coating using ^{1}H HR-MAS NMR spectroscopy

Fortunately, high-resolution Magic Angle Spinning (HR-MAS) NMR spectroscopy has been developed and proved to be very successful in investigating the ^{1}H NMR signals of functionalized shells of magnetic nanoparticles.[61] HR-MAS eases off the detrimental broadening caused by the presence of paramagnetic entities or viscous media by combining a specific set of parameters characteristic of NMR spectroscopy in solution with magic angle spinning (namely spinning the sample at a 54.7° angle with regard to the external static magnetic field) that is typical of solid-state NMR experiments. ^{1}H HR-MAS NMR experiments were performed to confirm the polyelectrolyte anchoring, infer the organization of the polyelectrolyte and especially PEG chains at the NA surface, and finally quantify the PEG grafting density, amenable to influence the surface interactions ruling cellular uptake. With this aim, systematic comparisons between free polyelectrolytes and functionalized NAs in D_2O solution were carried out. We considered for **P1** the protons of the acrylate chain (H_a and H_b) resonating between 1.5 and 2.5 ppm. For **P2** and **P3**, two sets of protons were scrutinized: methacrylate chains (H_{acr}) resonating between 1.5 and 2.2 ppm, and protons of the terminal methoxy (OMe) and methylene groups (OCH_2) of the PEG chains, resonating at 3.4 and 3.6 ppm respectively.

No change in the ratio for the H_a and H_b signal integrals was observed when comparing the NMR spectra of **P1** and **NA-P1** (Fig. S3). By contrast, the $I(H_{acr})/I(OCH_2)$ integral ratios of the methacrylate protons to the PEG protons notably decreased, namely by 11 and 16 % when evolving from the free polymers **P2** or **P3** respectively to the corresponding nanoconstructs **NA-P2** or **NA-P3** (Fig. S4 and S5). Such a decrease was even more discernable for the integral ratio $I(H_{acr})/I(OMe)$ that was reduced by 31 and 38 % when comparing the signals between **P2** and **NA-P2**, and **P3** and **NA-P3** respectively. Finally, the larger diminution of the integration ratio is worth noting for **P3** as compared to **P2**, suggesting substantial differences in the polyelectrolyte organization at the NA surface.

Table 2. Structural and photophysical characteristics of magneto-fluorescent **NA-Px** (x = 1, 2, 3) dispersions in water (except for TEM measurements).

NA-Px	D_Z (nm)[a]	PDI[a]	D_{TEM} (nm)[b]	ζ (mV)[c]	λ_{max}(abs) (nm)	λ_{max}(em) (nm)[d]	Φ_f (×10^{-2})[e]
NA-P1	167 ± 71	0.18	78 (0.22)	-40.2 ± 0.9	423	614	0.47
NA-P2	154 ± 53	0.12	75 (0.15)	-13.0 ± 1.1	429	591	0.20
NA-P3	234 ± 112	0.23	67 (0.13)	-12.3 ± 0.7	428	603	0.32

[a] Determined from DLS measurements in diluted dispersions from algorithms providing Z-average sizes; PDI designates the polydispersity index based on DLS intensity measurements. [b] Determined from TEM measurements and lognormal mathematical modelling after statistical counting of 200 nano-objects; σ designates the standard deviation. [c] Data from three independent measurements using zetametry. [d] Excitation performed at 460 nm. [e] Referred to coumarin 540A in absolute ethanol (Φ_f = 0.38).

Hence, the systematic reduction in the integration signals and the slight but reproducible +0.8 ppm downfield shift of the H_{acr} protons (highlighted with an asterisk on Fig. S4 and S5) in **NA-P2** or **NA-P3** as compared to those in **P2** or **P3** advocate for the firm attachment of **P2** and **P3** polyelectrolytes through the methacrylate units of their PMAA main chain, causing a loss of mobility of the latter. This also suggests extension of the PEG chains in water. This appears as a logical consequence of the large PEG hydration shell, contrarily to the hydrophobic and chelating main chain, trying to minimize solvation and extension in water by tightly wrapping the NA surface. The larger ratio decrease for **P3** with regard to **P2**, after coating the magnetofluorescent NAs, reasonably lets us assume a less compact PEGylated shell for **P3** at the NA surface and the corresponding structures depicted in Fig. 1B. This assumption nicely matches the larger mean hydrodynamic diameter D_Z observed for **NA-P3** at around 234 nm against 154 nm for **NA-P2**, namely below that found for **NA-P1** at 167 nm despite the absence of PEG chains. In order to gain insight in the comparative density and "compacity" of grafted **Px** chains at the nanoassembly surface, the number of grafted polyelectrolytes was estimated through quantitative ^{1}H HR-MAS measurements.

2.3 Quantification of the polyelectrolyte coating

Assessing the number of non-functional ligands anchored at the nanoparticle surface is usually performed using microscale thermogravimetry.[62] However, the herein investigated **NA-Px** are fabricated using a flash nanoprecipitation procedure that yields quite diluted systems and precludes the use of classical weight analyses. We resorted again to the highly sensitive ^{1}H HR-MAS technique and supplemented each **NA-Px** solution with a known amount of a deuterated 2,2,3,3-d_4(trimethylsilyl)propanoic acid (TSP), serving as an internal reference and a quantification standard. Thanks to the highly controlled structure of **P2** and **P3** achieved by RAFT polymerization, a quite accurate estimate of the number of grafted polyelectrolytes could be obtained, based on the integration of the TSP proton and PEG chain proton (OMe and OCH_2) signals that are less sensitive to iron oxide nanoparticles than those of acrylate protons. Considering a concentration of about 10^{10} NA per mL obtained from atomic force microscopy counting analyses performed on diluted dispersions, we calculated that around 3.4×10^7 **P1** chains, 2.5×10^6 **P2** chains, and 2.0×10^6 **P3** chains were coating the surface of **NA-P1**, **NA-P2** and **NA-P3** respectively. Such values nicely match former quantitative measurements performed on similar NAs, involving magnetic sedimentation and electrospray charge detection mass spectrometry.[54] A shell of 10^4 maghemite nanoparticles was then found, indicating that about one hundred polyelectrolyte chains surround each iron oxide nanoparticle composing the magnetic shell of **NA-P2** and **NA-P3**, which corresponds to a density of 0.16 and 0.12 chain per nm^2 for **P2** and **P3** respectively, if one considers the rough approximation of half of the SPIONs coated by the polyelectrolyte chains in the nanoassembly. The fact that the amount of **P1** chains *per* iron oxide nanoparticle for **NA-P1** is multiplied tenfold compared to that for **P2** and **P3** agrees with the much smaller polyacrylate chains, less subjected to steric crowding in the absence of PEGylated

View Article Online
DOI: 10.1039/D1NR06769A

brushes. Finally, given the very similar number of polyelectrolyte chains anchored at the **NA-P2** and **NA-P3** surface and the larger D_Z hydrodynamic diameter and PEG chain mobility for **NA-P3**, we could finally conclude from the above-conducted microscopic investigations that **P3** forms a less compact shell around the nanoassemblies than that displayed by **P2**. Since the latter comprises a slightly higher hydrophobic RAFT chain transfer agent through its alkylated end, larger structuration and segregation of the comb-like PEGylation shell would then be induced.

2.4 NA stealthiness toward blood cells

PEGylation is well known to reduce nano-object opsonization, consisting in the adsorption of blood proteins at the nanoparticle surface that promote their clearance by the mononuclear phagocytic system (MPS) and prevent long-term circulation.[63] Since the administration of nanomedicine is usually done intravenously, the first cells in contact with nano-objects are blood cells. Among them, lymphocytes and monocytes which possess a high phagocytic activity, represent important circulating populations involved in immune response. Therefore, the efficacy of NA PEGylation was assessed by measuring the rate of NA uptake by monocytes and lymphocytes using flow cytometry. Weak internalization of all NAs by lymphocytes was observed (RMFI values were found to be around 1.5, which corresponds to cell autofluorescence background) (Fig. 4A). In monocytes, internalization of **NA-P1** was twofold higher than that observed for the PEGylated NAs, namely **NA-P2** and **NA-P3** (Fig. 4B). No significant difference was observed between 6 and 24 h of incubation, which suggests fast NA uptake by cells. As expected, surface PEGylation of NAs reduced internalization by circulating monocytes, independently of their structure. This result suggests that PEGylated NAs like **NA-P2** and **NA-P3** could be appropriate for in vivo experiments and offer passive targeting by exploiting the enhanced permeability and retention effect (EPR) described in tumor.[64]

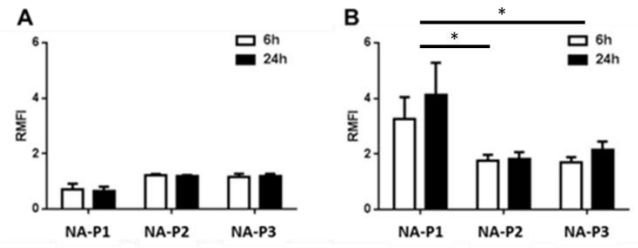

Fig. 4 Internalization of **NA-P1**, **NA-P2** and **NA-P3** by monocytes and lymphocytes from blood. PBMC from blood were incubated with **NA-Px** (x = 1,2,3 for 6 h or 24 h; then cells were analyzed using flow cytometry. Internalization of **NA-Px** by: A) lymphocytes, B) monocytes. Graphics represent the average ratios of mean fluorescence intensity (RMFI) +/- SEM obtained with PBMC from three different healthy donors. *p < 0.5.

2.5 Differentiated internalization of NAs by tumor cells

The absence of toxicity of NAs is the first crucial criteria to be considered for any further clinical transfer. In a previous study, **NA-P1** and **NA-P2** were found to be non-toxic for tumor cells[39] Interestingly, similar results were obtained with **NA-P3** on mesothelioma cell line Meso 11 and on adenocarcinoma cell line ADCA117, all derived from patients (Fig. S6), as a consequence of the seemingly structural similarities with **NA-P2**. Thanks to the NA bimodal imaging properties, permitted by the fluorescent core and SPION shell, studies of the NA internalization into cells resorted to experimental methods involving fluorescence measurement or nanoparticle tracking. We first performed a kinetic evaluation of NA internalization in Meso 11 and ADCA 117 cell lines using flow cytometry. NA detection started after 6 h of incubation. A plateau was reached for both cell lines after 24 to 39 h of incubation for all tested NAs (Fig. 5A-5B). Whereas the levels of internalized **NA-P1** and **NA-P2** were found to be similar, a threefold higher RMFI was obtained with **NA-P3**, which could not originate from a higher fluorescence quantum yield Φ_f that was actually measured for NA-P3 and found to be between those of **NA-P1** and **NA-P2** (Table 2). The influence of the surface charge, observed for negative/neutral and positive nanoparticles,[65] to explain differentiated internalization has also to be ruled out in our case for two reasons. First, the ζ potential values were measured to be equal for **NA-P2** and **NA-P3**. Second, even though **NA-P1** and **NA-P2** have different ζ potential values (-44 mV and -12 mV, respectively), their internalization kinetics were found to be similar. Since the NA sizes are in the same range and their surface potential exerts no effect, we can reasonably consider that surface structural parameters could play a major role in the NA ability to enter cells. A recent study has evidenced the neat reduction of cell uptake for PEGylated gold nanoparticles comprising terminal dodecyl units at only a 0.2 % mass fraction.[66] In our case, the contribution of the thioalkyl chain in **P2** represents a quite similar mass fraction at 0.5 %. Nevertheless, the herein reported architectures display PEG chains that are 10 times longer (~14 nm) than the dodecyl unit (~1.4 nm) of the incorporated RAFT CTA. Moreover, the comb-like **P2** and **P3** architectures favour PEG exposure around the NA surface, preventing the hydrophobic Z group from directly interacting with the cell membrane. Following the above-mentioned spectroscopic analyses evidencing neat structural differences between **NA-P2** and **NA-P3**, we are prompted to propose the existence of a more compact PEGylated shell in **NA-P2** as a possible explanation of the lesser cell uptake of **NA-P2** compared to that for **NA-P3**. Hence, higher structural reorganization energy of the NA shell upon interacting with the cell membrane would be required, decreasing their uptake.[30,67] This result points out the fact that simply evoking hydrophobic effects when comparing the influence of RAFT CTAs may not be sufficient and requires more accurate description of the chain arrangements.[68] This echoes a recent study concluding that not only the hydrophobicity, but also the distribution of monomers in RAFT polymers, and the resulting structuration have to be thoroughly regarded to interpret their effect on cell uptake.[69]

Finally, in order to prove NA cell internalization, confocal fluorescence microscopy was performed and showed the exclusive presence of NAs inside both thoracic tumor cell lines (Fig. 5C-5D). Orthogonal projections additionally pointed out the absence of NAs in the cell nuclei, which agrees with the absence of significant cell toxicity. TEM investigations were performed to prove the internalization of the whole core-shell NAs and gain insight into the subcellular NA localization inside cells. **NA-P2** and **NA-P3** were found localized into endocytic vesicles after 24 h of incubation (Fig. 6A-6B), following the same subcellular localization as that already reported for **NA-P1** in earlier studies.[39] Here, no particular fate difference as a function of the RAFT CTAs could be noticed after uptake, letting

suggest that membrane crossing would represent a crucial determining step. The organization of SPIONs following a raspberry-like architecture thus suggests that the NA structure was maintained in the subcellular compartments after 24 h of internalization.[70]

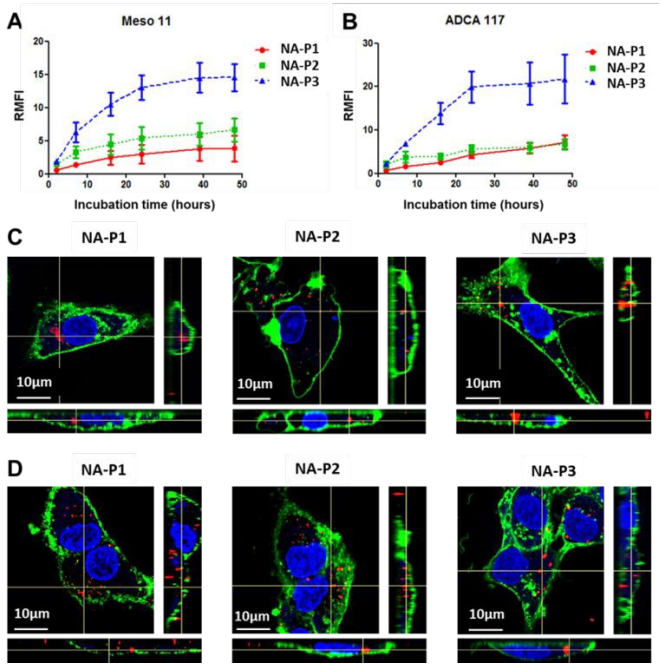

Fig. 5 Internalization of **NA-P1**, **NA-P2** and **NA-P3** by thoracic tumor cell lines. MPM (A-C) and lung ADCA (B-D) cells were incubated with **NA-Px** (x = 1,2,3. A) and B) kinetic of **NA-Px** internalization analysed using flow cytometry. Graphics represent the average ratios of mean fluorescence intensity (RMFI) +/- SEM obtained from three independent experiments. C) and D) Confocal fluorescence microscopy.

To conclude, the exploitation of the multimodal imaging properties of NAs allowed to demonstrate the conservation of their MRI properties as dark contrast agents after cell internalization. Whereas Meso11 and ADCA117 cells serving as control cells appeared white, pellets of cells incubated with NAs appeared black due to a high contrast induced by the presence of iron oxide nanoparticles in cells (Fig. 6C-6D).

2.6 Self-disassembling of NAs for short-term accumulation

Any novel nanomedicine development requires today the strict absence of bioaccumulation either through kidney clearance for ultra-small nanoparticles or biodegradation and assimilation for larger nanoparticles. Moreover, for further drug delivery, nanoparticle erosion or disassembling stimulated by enzyme, chemicals or physical stimuli, is a high pre-requisite. At the beginning of the internalization process, we observed the presence of yellow/orange dots for all tested NAs in both Meso11 and ADCA117 cell lines, indicating colocalized NAs (red) and lysosomes (green). These observations are in line with the endocytotic internalization pathways generally involved in nanoparticle internalization. Indeed, nanoparticles usually undergo active endocytosis through pinocytosis, involving or not clathrin receptors, and mostly resulting in localization in lysosomes.[71-72] After a 24 h-long period of cell incubation and several washing steps, we noticed a progressive shift of the fluorescence intensity at 670 nm corresponding to the spectral range where the fluorophores self-assembled in NAs mostly emit. The hypsochromic emission shift, measured by using flow cytometry at 530 nm, results from NA disassembling into individual subunits that are solvated by lipid surroundings.[73-74] Hence, NA degradation could be tracked by the ratio of 530 to 670 nm intensities that decreased as soon as NAs disintegrate. The initial ratios were found to be quite different for **NA-P2** due to the fact that the NA emission spectrum shifted to lower wavelengths (Table 2).

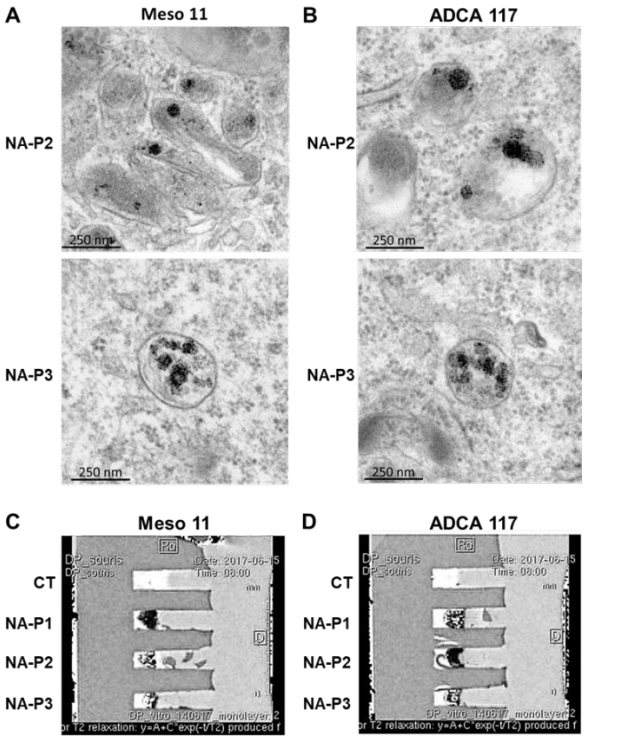

Fig. 6 Visualization of the iron oxide nanoparticles of the internalized **NA-Px** (x = 1,2,3). MPM (A-C) and lung ADCA (B-D) cells were incubated with the different **NA-Px**. A) and B) TEM pictures of Meso 11 control cells (CT) and cells incubated with the magneto-fluorescent **NA-P1**, **NA-P2**, and **NA-P3** for 24 h. C) and D) T2* map of MRI images.

In both cell lines, all ratios decreased progressively over time, thus suggesting slow NA degradation which appeared to be independent of the NA structure (Fig. 7).

View Article Online
DOI: 10.1039/D1NR07769A

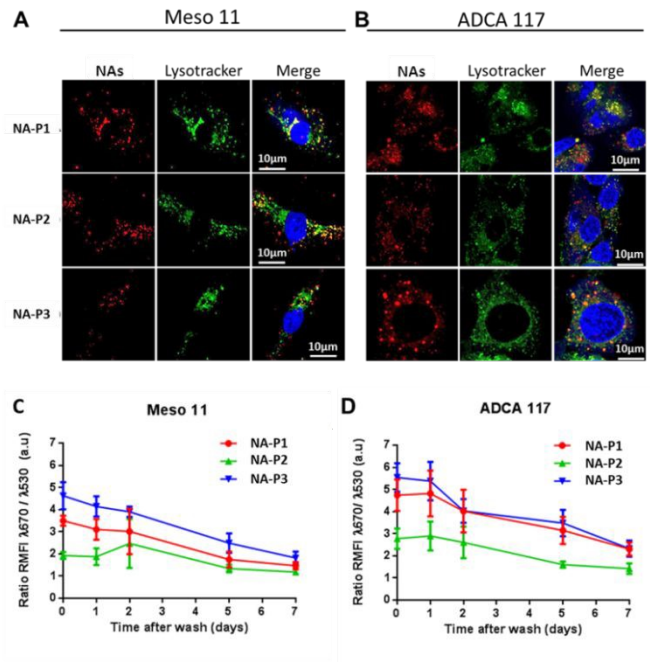

Fig. 7 Intracellular localization and degradation of **NA-P1**, **NA-P2** and **NA-P3**. MPM (A-C) and lung ADCA (B-D) cells were incubated with **NA-Px** (x = 1,2,3). A) and B), pictures obtained using confocal microscope. Red: **NA-Px**; Green: lysosome; blue: nuclei; and yellow/orange: colocalization. C) and D), degradation of **NA-Px** over time, evaluated by calculating the ratio of RMFI of fluorescence at 670 nm to RMFI of fluorescence at 530 nm measured using flow cytometry. Graphics represent ratio of mean fluorescence intensity (RMFI) +/- SEM obtained from three independent experiments.

This observation is actually compatible with the delivery kinetics of doxorubicin observed in a previous study using fluorescent NAs.[59] Indeed, labelling of cell nuclei by doxorubicin was delayed by 24 h compared to free molecule in accordance to the kinetics of NA degradation recorded in this study.

2.7 NA diffusion in 3D cell culture models ruled by cell compaction

In the pathophysiological situation, tumor cells are organized in three dimensions, which generates physical barriers and constraints for the free-diffusion of therapeutics, including nanomedicine, inside the structure. To reproduce these constraints, cells were grown in non-adherent conditions and round bottom wells to induce the formation of multicellular spheroids (MCTS) (Fig. S7). Considering MCTS of various sizes illustrates the natural heterogeneity encountered in patients' tumors. Using confocal microscopy after clarification of MCTS, we observed the presence of NAs at the center of Meso 11 MCTS (Fig. 8 left panels), whereas all NAs appeared located only at the periphery of ADCA 117 MCTS (Fig. 8 right panels). We expanded the former experiments to a second model of MPM forming compact MCTS, Meso 13 (Fig. S7 and S8). Interestingly, as observed for ADCA 117, NAs did not diffuse at all inside Meso 13 MCTS (Fig. S8). An explanation could be the compaction of the 3D structures which depend on cell interactions and matrix production. These results point out the important fact that fibrotic tissues, mimicked by MTCS, can face hampered nanoparticle diffusion, and become inappropriate models to assess the efficacy of nanomedicines. Hence, careful choice of cells is to be considered for therapeutic approaches based on nanomedicines requiring deep drug diffusion into tissues. This in turn opens questions on the structural characteristics of nanoparticles that need to display large diffusion in complex environment cancer 2D-3D.[75]

2.8 Privileged internalization of NAs as a function of the macrophage subtype of the tumor microenvironment

Tumor tissues are complex and composed of different cell types. Macrophages are usually observed in the tumor microenvironment and contribute to tumor progression. They are classically divided in two main subtypes, M1 macrophages with antitumoral activity and M2 macrophages with immunosuppressive and protumoral properties.[76-77] First, we aimed at evaluating the behaviour of all three NAs on M1-like and M2-like macrophages, phenotypically characterized by measuring CD14 and CD163 expression using flow cytometry (Fig. S9A-S9B). All NAs were found to be more efficiently internalized by M2-like macrophages compared to M1-like macrophages (approximately 2 fold) (Fig. 9A), which reflects the expected high phagocytic ability of M2-like macrophages.[78] We thus focused our analysis on M2-like macrophages which have recently appeared as a very promising therapeutic target in oncology. [79]

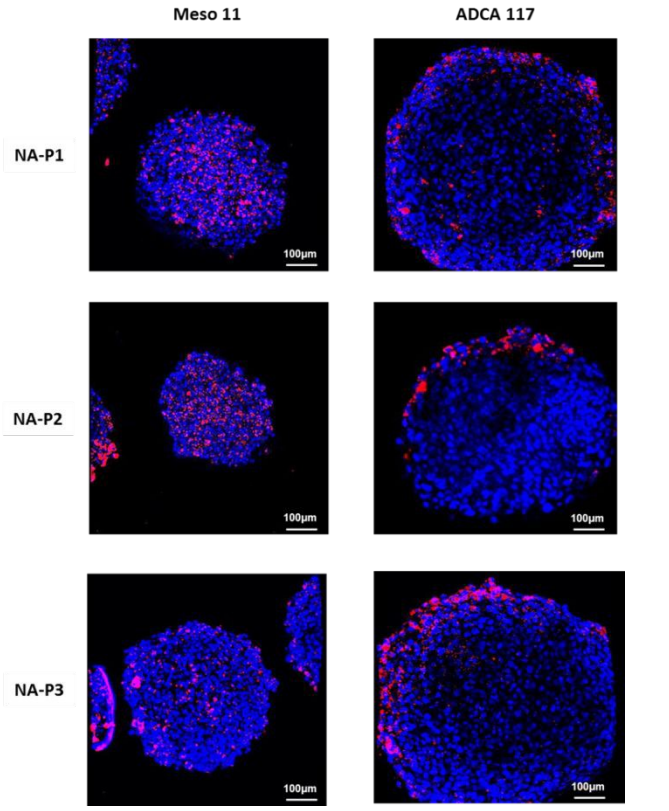

Fig. 8 Internalization **of NA-P1**, **NA-P2** and **NA-P3** by cells cultured as MCTS. MPM (Meso 11) and lung ADCA cells (ADCA 117) were cultured as MCTS and incubated with **NA-P1** (A) or **NA-P2** for 24 h. Pictures were obtained using confocal fluorescence microscopy. Blue: nuclei, pink: **NA-Px**.

While internalization of all NAs after 24 h was proved by confocal fluorescence microscopy (Fig. 9C), kinetic studies showed a regular increase in NA accumulation in M2-like macrophages over time

before reaching a plateau after 39 h of incubation (Fig. 9B). Similarly to the results obtained in tumor cells, **NA-P3** was found to be the most internalized compared to **NA-P2** and **NA-P1** (7- and 2-fold higher amounts respectively) (Fig. 9B). The lower internalization rate of **NA-P2** displaying a more compact PEGylated shell agrees with the reduced phagocytosis reported for chitosan nanoparticles coated with a low density of long PEG ligands, allowing for a smaller hydrodynamic diameter and enhanced compacity.[23]

Contrary to the latter study where reduction in the surface potential promoted low nanoparticle uptake by macrophages, no charge effects could be advocated in our case since the zeta potentials of both **NA-P2** and **NA-P3** were found very similar at around -13.0 and -12.3 mV respectively. This reinforces our assumption that structural, rather than purely electrostatic effects underpin the microscopic interactions between the nanoassemblies and macrophages. Along these lines, recent studies have indeed evidenced that 9 nm-large SPIONs coated with cyclic PEG ligands, forming dense brushes, repelled serum proteins, like albumin, very efficiently compared to linear PEG ligands, which in turn ensures low phagocytosis.[80] This was also demonstrated with 200-300 nm large ovalbumin nanocapsules whose stealth properties and phagocytotic inhibition toward immune cells are considerably improved by surface functionalization with densely packed PEG brushes.[81] Interestingly, M2-like macrophages display higher internalization rates of PEGylated NAs than those obtained with MPM cells as revealed by flow cytometry. Indeed, macrophages compared to tumor cells display a 2-fold, 4-fold and 3-fold higher RMFI signals for **NA-P1**, **NA-P2** and **NA-P3**, respectively. To confirm the higher capacity of M2-like macrophages to engulf NAs, MPM cells were co-cultured with M2-like macrophages and added with NAs for 24 h.

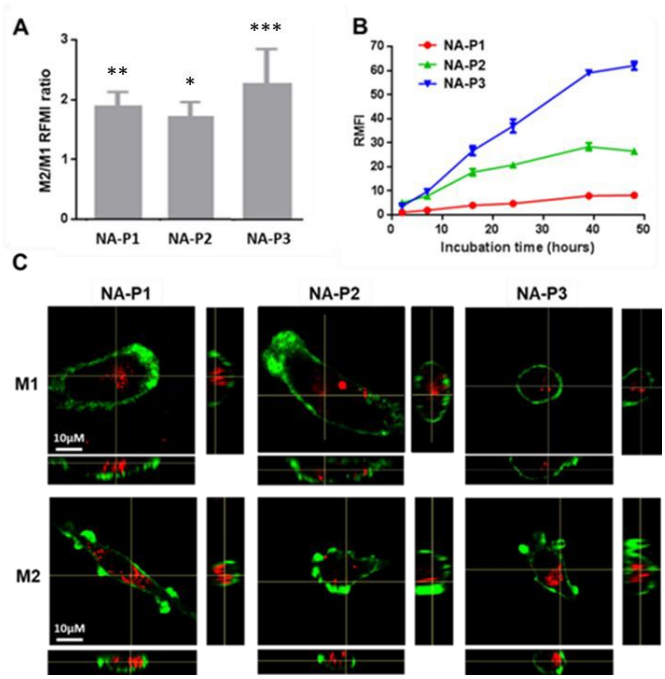

Fig. 9 Internalization of **NA-P1**, **NA-P2** and **NA-P3** by macrophages. A) M1-like and M2-like macrophages were incubated with **NA-Px** for 24 h and analyzed using flow cytometry. M1 vs M2: *p < 0.05; **p < 0.001; ***p < 0.0001. B) Kinetics of **NA-Px** internalization by M2-like macrophages. Graphics represent the average ratios of mean fluorescence intensity (RMFI) +/- SEM obtained from three independent experiments. C) Confocal fluorescence microscopy images, with orthogonal projections, of M1- and M2-like macrophages incubated with NAs for 24 h. Green: membranes, and red: **NA-Px** (x = 1,2,3).

Confocal fluorescence microscopy nicely confirmed our assumptions with a higher amount of NAs and in particular **NA-P3** internalized in M2-like macrophages (Fig. 10).

Finally, we examined the interactions of primary healthy mesothelial cells (MC) with NAs surrounding MPM tumors which is paradoxically often overlooked despite its utmost importance when considering preliminary cell tests. Indeed, MPM tumors arise from the pleura and grow in the pleural cavity. Thus, as a prospective treatment, injections in this cavity could naturally be envisaged in order to have direct access to tumor cells and gain efficacy.[82] MC and two MPM cell lines (Meso96 and Meso11) serving as controls, were thus been exposed to NAs during 24 h. NA internalization was then monitored and analyzed using flow cytometry and confocal fluorescence microscopy (Fig. S10). **NA-P3** appeared again to be the most internalized NAs by cells. However, the differences between both healthy and malignant cells are not statistically significant enough (Fig. 11).

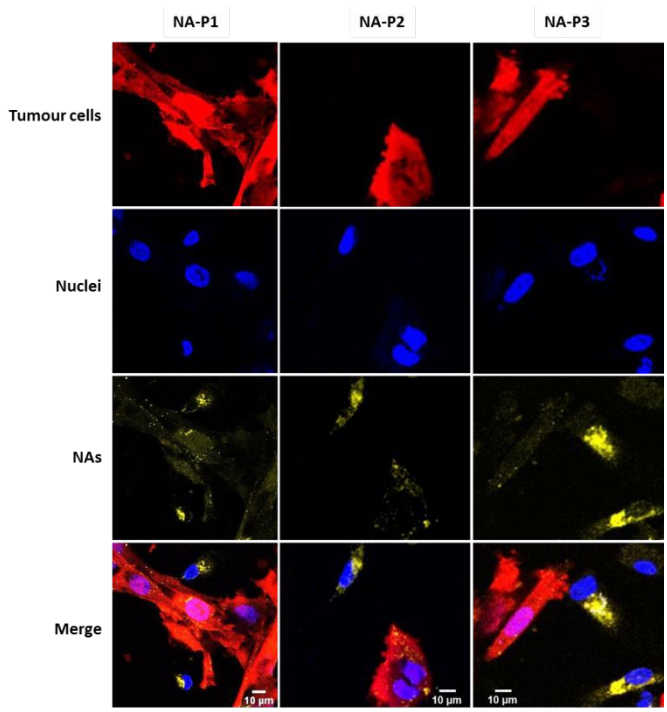

Fig. 10 Internalization of **NA-P1**, **NA-P2** and **NA-P3** by tumor cells and macrophages in co-culture. Meso 34–Ruby cells were co-cultivated with M2-like macrophages and incubated for 24 h with **NA-P1**, **NA-P2** or **NA-P3**. Pictures were obtained using confocal microscope. Red: tumor cells; blue: nuclei; and yellow: **NA-Px** (x = 1,2,3).

The tendency for all PEGylated NAs to address more specifically MPM cells comparatively to primary mesothelial cells nevertheless casts no doubt. This control, rarely performed with healthy cells, reveals the need for targeting ligands or proteins at the nanoparticle surface, that are specific to tumor cells, in order to improve the efficacy of nanomedicines.[83-84]

View Article Online
DOI: 10.1039/D1NR06760A

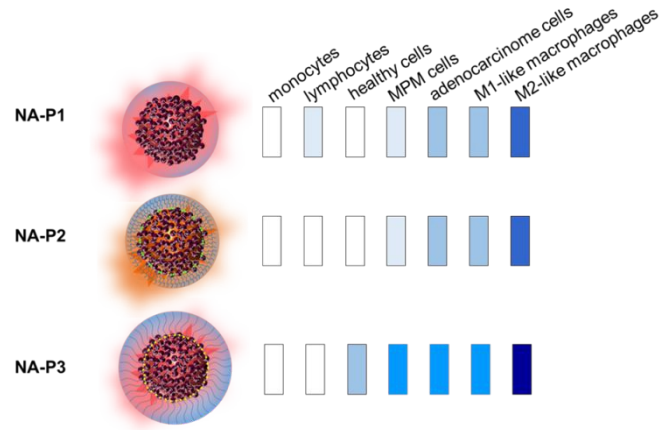

Fig. 11 Comparative uptake of **NA-Px** (x= 1,2,3) by blood, healthy, cancer and immune cells. The darker the color, the higher the endocytotic capability of the cells.

3. Experimental section

3.1 Polymer synthesis and characterizations

3.1.1 Materials. Azobisisobutyronitrile (AIBN; Sigma-Aldrich; 98 %) was recrystallized twice from methanol prior to use. Poly(acrylic acid) (PAA) (average Mn 1800 g.mol^{-1}) (**P1**), poly(ethylene glycol) methyl ether methacrylate (average M_n 2000 g.mol^{-1} at 50 wt. % in H_2O) ($MAPEG_{2000}$), methacrylic acid (MAA; 99 %), and 2-cyano-2-propyl benzodithioate (CPBDT; 97 %) were purchased from Sigma-Aldrich (St Quentin Fallavier, France) and used as received. The synthesis of **P2** using 2-cyano-2-propyl dodecyl trithiocarbonate as a RAFT transfer agent was earlier reported in literature.[39]

*3.1.2 Synthesis of **P3** poly(MAA-stat-$MAPEG_{2000}$).* The targeted molar fraction in MAA was 80 %. 5.1 mg of AIBN (3.1×10^{-2} mmol, 0.25 eq.), 27.4 mg of CPBDT (1.24×10^{-1} mmol, 1 eq.), 215 mg of MAA (2.49 mmol, 20 eq.), 2.503 g of the solution of $MAPEG_{2000}$ at 50 wt. % in water (0.50 mmol, 5 eq.), and 634 mg of water were placed in a Schlenk flask. Note here that a higher AIBN/CPBDT ratio than usual was used to get rid of the inhibitors present in the monomer solutions, reacting first with AIBN. The solution was thoroughly deoxygenated by three freeze-pump-thaw cycles. The flask was filled with nitrogen gas and placed in an oil bath maintained at 85 °C for 5 h under magnetic stirring. The time reaction was chosen so as to avoid undesirable termination reactions or uncomplete MAA monomer consumption. The sample was dried upon solvent removal under reduced pressure.

3.1.3 Polymer characterizations. Analysis by ^{1}H NMR (Varian Mercury, 300 MHz) provided the number average molecular weight M_n. Monomer conversion, molecular weights and dispersity were determined by size exclusion chromatography (SEC) in DMF containing LiBr at a concentration of 10 mmol.L^{-1}. Solutions of samples with concentrations around 5 mg.mL^{-1} were prepared and filtered (PTFE membrane; 0.20 µm) before injection. The flow rate was 0.9 mL.min^{-1} (50 °C). The following Agilent 1260 Infinity (Agilent, les Ulis) series setup was used: a G1310B isocratic pump; a G1322A degasser; a G1329B auto-sampler; a G1316A thermostated column compartment equipped with a set of Polymer Laboratories PLgel columns (nominal particle size: 5 µm) composed of a guard column (50×7.5 mm) and two MIXED-D columns (300×7.5 mm); a G1314B variable wavelength detector; and a G7800A multidetector suite equipped with a MDS refractive index detector. Calibration was performed using a set of EasiVial polystyrene PS-M standards purchased from Agilent and served for determining the molecular weight distributions. Monomer conversion was assessed from SEC titrations implying $MAPEG_{2000}$ solutions with varying concentrations and integration of the corresponding eluted peaks.

3.2 Fabrication and structural characterizations of magneto-fluorescent nanoassemblies

3.2.1 Nanoassembly synthesis. A solution of phosphonic acid fluorophores[54] in THF (50 µL, 0.1 wt. %) was added under vortex mixing to a diluted nitric acid solution of maghemite nanoparticles (2.5 mL, pH = 1.2, 0.006 wt. %). Then, the resulting magneto-fluorescent NAs were subsequently stabilized with the retained polyelectrolyte and the solution pH raised to neutral. With this aim, the corresponding polyelectrolyte was added as a powder (5 mg for **P1**, 17 mg for **P2**, 17 mg for **P3**), and the pH of the solution adjusted to 9 by adding dropwise an ammonium hydroxide solution (1.3 mol.L^{-1}). The resulting dispersion was allowed to stir for a further 30 min and dialyzed using a Spectra Por membrane (standard grade regenerated cellulose; 8−10 kDa MWCO for **P1**, and 300 kDa MWCO for **P2** and **P3**) against Millipore water (600 mL) for over 24 h to remove excess polymers and reach neutral pH. The resulting solution was divided in 2 mL fractions into small vials and lyophilized. The vials were finally stored at −18 °C until solution reconstitution (total volume 2 mL) with water, phosphate-buffered saline (PBS), or a cell culture medium depending on the planned biological investigations.

3.2.2 Size measurements. Dynamic light scattering measurements were carried out at 25 °C by means of the Vasco 3 size analyzer (Cordouan Technologies, Pessac, France), equipped with a 40 mW laser diode operating at 658 nm. All data were collected in a backscattering mode at an angle of 135°. For each sample, intensity measurements were carried out in a multi-acquisition mode implying automatically adjusted correlograms and averaged measurements on six acquisitions. Z-averaged hydrodynamic diameter (DZ) and polydispersity index (PDI) were obtained by fitting each correlogram with a Cumulant-based algorithm provided by Cordouan Technologies. Measurements of surface potential ζ, were carried out by means of a Zetasizer Nano ZS ZEN 3600 (Malvern, Orsay, France). The samples were placed in disposable folded capillary cells (DTS1070). Three measurements were performed for each sample and the zeta potential was calculated from electrophoretic mobility dispersion fitted by the Smoluchowski model. TEM analyses were performed using a MO-Jeol 1230 operated at 80 kV. All nanoassembly solutions were deposited onto holey carbon-coated copper grids (300 mesh). The mean diameter (D_{TEM}) and standard deviation (σ) were assessed by fitting with a lognormal distribution the histograms issued from counting 200 nano-objects using the free ImageJ software. The quality of the sample and especially the possibility of aggregation in the case of NA-Px can be due to the sample concentration, rate of the drying process, and interactions on the surface after drop-casting on the carbon-coated grids.

3.3 Spectroscopic characterizations in solution

3.3.1 Photophysical properties. UV−visible absorption spectra were recorded using a Cary 5000 spectrophotometer (Agilent, les Ulis,

France). Steady-state emission spectra were recorded using a Fluorolog 3 spectrofluorometer (Horiba, Longjumeau, France). Correction for the emission spectra with regard to the spectral response of the detector was automatically applied. Fluorescence quantum yields were determined in solution, referred to coumarin 540A in ethanol (Φ_f = 0.38).

3.3.2 ^{1}H HR-MAS NMR investigations. Lyophilized **NA-P1**, **NA-P2** and **NA-P3** samples were redispersed in D_2O (60 mL) and a 1.71 mmol.L^{-1} TSP solution in D_2O (30 mL) was added. Solutions of free **P1**, **P2** and **P3** were prepared at a 17.3, 7.6, and 5.0 mmol.L^{-1} concentration, respectively. ^{1}H HR-MAS NMR spectra were recorded using Avance II-spectrometer (Bruker, Karlsruhe, Germany) working at 500 MHz, with a spinning rate of 5000 Hz for all samples. The water peak suppression was achieved through the noesypr1d sequence.

3.3.3 Polymer chain quantification. Quantification of the polymer chains around the nanoassemblies was performed using a TSP solution in D_2O at a known concentration, mixed to a given volume of **NA-Px** dispersion in D_2O. By comparing the peak areas of TSP with those of the -OMe groups of the PEG chains of **P2** or **P3** around the nanoassemblies and taking into account the respective number of protons for each entity, one could infer the concentration of PEG chain, and the total concentration of the corresponding polymer present in the NMR tube. As for NA-P1 coating, the acrylic proton signals were integrated and referred to TSP ones to infer the concentration of **P1**. The number of polymer chains per nanoassembly was then directly calculated by dividing the known number of moles of polymer chains in solution by the NA number of found to be around 10^{10} per mL from AFM measurements. Hence, 3.4x10^7 **P1**, 2.5x10^6 **P2** and 2.0x10^6 **P3** chains were found to coat **NA-P1**, **NA-P2**, and **NA-P3** respectively.

3.4 Cell culture

3.4.1 Malignant cell culture. The mesothelioma cell lines (Meso 11, Meso 13 and Meso 96), and the lung adenocarcinoma cell line (ADCA 117), were established from pleural effusion of patients,[85] and belong to a validated biocollection (Ministère de l'Enseignement Supérieur et de la Recherche n° DC-2011-1399 and Commission Nationale de l'Informatique et des Libertés (CNIL) n°: 1657097). These cells were characterized for the mRNA expression of the usual MPM markers used for immunohistochemistry and for their mutational status using targeted sequencing. All cell lines were maintained in RPMI 1640 medium (Gibco®, Thermo Fisher Scientific, France) supplemented with 2 mmol.L^{-1} L-glutamine (Gibco®, Thermo Fisher Scientific, France), 100 U.mL^{-1} penicillin, 100 µg.mL^{-1} streptomycin and 10 % of heat-inactivated fœtal calf-serum (Dominique Dutscher, Bernolsheim, France) and cultured at 37 °C in 5 % CO_2 atmosphere. Primary peritoneal mesothelial cells (MES-F) were purchased from (Zen Bio®, UK) and maintained in culture with Medium 199 (Sigma-Aldrich, St Quentin Fallavier, France) supplemented with 100 U/mL penicillin, 100 µg.mL^{-1} streptomycin and 10 % of heat-inactivated fœtal calf-serum (Gibco®, Thermo Fisher Scientific, France).

3.4.2 Three-dimensional (3D) cell culture – Multi cellular tumor spheroids (MTCS). Cells were seeded in Nunclon Sphera 96-well microplate (Thermo Fisher Scientific France) at a density of 2×10^4 cells per well in 180 µL of culture medium. They were centrifuged at 800 g for 1 min. After 72 h of incubation at 37 °C and 5 % CO_2, the 3D structure was established.

3.4.3 Differentiation of monocytes into macrophages. Monocytes, obtained by elutriation (DTC platform, Nantes, France), were seeded in 6-well plates at a density of 5×10^6 cells in 5 mL of culture medium. To obtain M1-like macrophages, the medium was supplemented with granulocyte-macrophage colony-stimulating factor (GM-CSF) at 20 ng.mL^{-1} (Cellgenix, Freiburg, Germany). To obtain M2-like macrophages, the medium was supplemented with macrophage colony-stimulating factor (M-CSF) at 50 ng.mL^{-1} (Isokine, Kopavogur, Iceland)84 during 3 days at 37 °C in 5 % CO_2 atmosphere.[86] Then, M1-like and M2-like macrophages were collected and labelled with anti–CD14–fluorescein-isothiocyanate (FITC) (Beckman Coulter, Fullerton, CA) and anti–CD163- allophycocyanin (APC) (R&D Systems®, Bio-Techne, Lille, France) antibodies or IgG2a-FITC (Beckman Coulter, Villepinte, France) and IgG1-APC (R&D Systems) isotype controls respectively. Viability was assessed using TO-PRO-3 Iodide 642/661 at 1 µmol.L^{-1} (Thermo Fisher Scientific France). Analysis of the cells was performed using flow cytometry (FACSCalibur; Becton Dickinson, Rungis, France). Expressions of CD14 and CD163 were analyzed with FACS Flowjo Software (Tree Star Inc®, USA).

3.5 Cell internalization and fate of the nanoassemblies

3.5.1 Endocytosis by tumor cells. Tumor cells were seeded at a density of 5x10^4 cells per well of 12-well plates (Falcon®, Dominique Dutscher, France), primary mesothelial cells (MES-F) and differentiated macrophages were seeded at a density of 1x10^5 cells per well of 12-well plates (Falcon®) and incubated at 37°C during 24 h. Then, **NA-Px** solutions (40 µL, 4×10^8 NAs) after redispersion in the appropriate medium (2 mL) were added on cells for the indicated period of time. The wells were washed once with PBS. The cells were harvested after incubation with Trypsin-0.05 % EDTA (Gibco®, Thermo Fisher Scientific France) and centrifuged during 60 seconds at 800 g in an Eppendorf Minispin (Thermo Fisher Scientific France). They were resuspended in PBS and analyzed using flow cytometry (FACSCalibur, Becton Dickinson, Rungis, France). Ten thousand events were acquired and analyzed with Flowjo Software (Tree Star Inc®, USA).

3.5.2 Internalization by monocytes and lymphocytes. Blood samples were collected from healthy donors (EFS, French Blood Authority). PBMCs were isolated using Ficoll gradient (Eurobio, les Ulis, France). The cells were resuspended in RPMI 1640 medium (Gibco®, Thermo Fisher Scientific France) supplemented with 2 mmol.L^{-1} L-glutamine (Gibco®, Thermo Fisher Scientific France) 100 U.mL^{-1} penicillin, 100 µg.mL^{-1} steptomycin and 10 % of heat-inactivated fœtal calf-serum (Dominique Dutsher, Bernolsheim, France). PBMCs were seeded at a density of 2.5×10^6 cells in 5 mL of culture medium in wells of 6-well plates (Nunc, Dominique Dutscher, France). NA dispersions (40 µL, 4×10^8 NAs) were added for 6 or 24 h at 37 °C in 5 % CO_2 atmosphere. The cells were harvested and centrifuged during 5 minutes at 800 g. The supernatant solutions were removed and the cells resuspended in PBS. All samples were analyzed using flow cytometry (FACSCalibur, Becton Dickinson, Rungis, France) after addition of 1 µmol.L^{-1} TO-PRO-3 Iodide 642/661 (Thermo Fisher Scientific France). Monocyte and lymphocyte populations were identified using FSC/SSC

parameters. The results were analyzed with Flowjo Software (Tree Star Inc®, USA).

3.5.3 Degradation of the nanoassemblies in tumor cell lines. Cells were seeded at the density of 5×10^4 cells per well of 12 well-plates. After 24 h, solutions (40 µL, 4×10^8 NAs) of lyophilized **NA-Px** samples redispersed in PBS (2mL) were added in wells and left for 1 day. The wells were then washed once with PBS and 2 mL of new culture medium were added before incubating the plates for an additional 2 to 5 days at 37 °C. At the end of each incubation time, the cells were harvested after treatment with Trypsin-0.05 % EDTA (Gibco®) and centrifuged during 60 seconds at 800 g. They were resuspended in PBS and analyzed by flow cytometry (FACS Calibur, Becton Dickinson, Rungis, France). Ten thousand events were acquired and analyzed with Flowjo Software (Tree Star Inc®, USA).

3.6 Live cell imaging using confocal microscopy and MRI, and TEM imaging of fixed cells

3.6.1 Confocal microscopy. Meso 11, ADCA 117, and primary mesothelial cells (MES-F) were respectively seeded at a density of $2x10^4$, $1x10^4$ and 10^4 cells per well of µ-slide 8-well ibitreat microscopy chamber (Ibidi®, Biovalley, llkirch-Graffenstade, France) and incubated at 37 °C during 24 h. For co-culture experiments, $1.4x10^4$ Meso 34-ruby cells and 0.6×10^4 M2-like macrophages were seeded per well of µ-slide 8-well ibitreat microscopy chamber (Ibidi®, Biovalley, llkirch-Graffenstade, France) and incubated at 37 °C during 24 h. Then, **NA-Px** dispersions (10 µL, 1×10^8 NAs) were added for 24 hours. For internalization experiments, cells were labelled using wheat germ agglutinin (WGA)-AlexaFluor® 647 probes (Molecular Probes®, Thermo Fisher Scientific France) at 5 µg.mL^{-1} for 10 minutes at 4°C. For colocalization experiments, the cells were labelled using Lysotracker Deep Red (Molecular Probes, Thermo Fisher Scientific France) at 25 nmol.L^{-1} for 1 h at 37 °C. The supernatants were removed and new culture medium was added. The cells were fixed during 20 min at room temperature using a solution containing paraformaldehyde (PFA) 4% (EMS, Hatfield, PA, USA) and Hoechst 33342 (Sigma-Aldrich, St Quentin Fallavier, France) at 5 µmol.L^{-1} in order to stain the nuclei,. They were washed with PBS and nucleus fluorescence imaging was performed using a Nikon A1R Si confocal fluorescence microscope, equipped with Ar^+ and He-Ne lasers as excitation sources and a Plan Apo oil-immersion objective (60×; NA = 1.4, DICIII). For 3D structures, MCTS were fixed with PFA 4% containing 10 µmol.L^{-1} Hoechst 33342 for 16 h. They were washed once with PBS and permeabilized during 24 h with PBS containing 2 % Triton X100 at RT. This solution was removed and MCTS were resuspended into a RapiClear solution (SunJin Lab, Hsinchu City, Taiwan) supplemented with 10 µmol.L^{-1} Hoechst 33342 and observed with a confocal microscope (Nikon A1R Si, 20×; NA = 0.7).

3.6.2 Magnetic resonance imaging (MRI). A scaffold was designed according to a glass cylinder (54mm×27mm). The ghost background was filled with 1 wt. % low-melting agarose gel (Sigma-Aldrich, St Quentin Fallavier, France) and two rows of four wells were created thanks to a 3D-printed plastic comb. Monolayer Meso 11 cells were seeded on the first-row wells at a density of $2x10^5$ cells per well in PBS. Monolayer ADCA 117 cells were seeded on the first-row wells at a density of $2x10^5$ cells per well in PBS. The top of the scaffold was filled with a 1 wt. % low-melting agarose gel. All MRI studies were performed with a Biospec Avance III MR scanner (Bruker Biospin, Wissembourg, France) using a 20 cm bore 7 T magnet equipped with BGA12S gradient/ shim system capable of 675 mT.m^{-1} maximum gradient strength. A 35-mm-diameter volume coil was used.

3.6.3 Transmission electron microscopy (TEM). Meso 11 and ADCA 117 cell lines were incubated with NA dispersions (40 µL, $4x10^8$ NAs) during 24 h at 37 °C in 5 % CO_2 atmosphere. Cells were collected and fixed in Trump's solution. They were post-fixed with 2 % osmium tetroxide (EMS, Hatfield, PA, USA), dehydrated with a series of increasing ethanol solutions, and embedded in Epon®resin (Sigma; Steinheim, Germany). Ultrathin sections (90 nm) were stained with 2 % aqueous uranyl acetate and 1 % lead citrate (Merck, Darmstadt, Germany). Images were acquired using a JEOL 1011 transmission electron microscope operating at 100 kV.

3.7 Statistical analyses

For cytometry experiments, three independent experiments were performed and the results were expressed as the average ratios of mean fluorescence intensity (RMFI) +/- Standard Error of the Mean (SEM). Comparisons were performed using unpaired t-test or ANOVA followed by Tukey's multiple comparisons test for comparison of more than 2 conditions. All statistical analyses were done using GraphPad Prism (Prism V.6 for Windows).

Conclusions

In this study, we have designed various red-emissive magneto-fluorescent nanoassemblies differing by their sole outer polyelectrolyte shell issued from RAFT comb-like PEGylated polymers, to assess the impact of the chain transfer agent on cell uptake. Photophysical studies and ^{1}H HR-MAS NMR investigations in solution were efficient tools to reveal distinct structuration of the PEGylated chains around the nanoassemblies, leading to a more compact shell for chain transfer agents incorporating an extended alkyl activating group, amenable to self-assemble in close contact with the NA surface. Systematic cell uptake experiments carried out on different human cellular models from tumor microenvironment, evidenced neat differences between the PEGylated nanoassemblies despite the very slight changes induced by the activating group and their identical surface potential. In a general way, the nanoassemblies, displaying the denser PEG shell, were internalized the less following a classical endocytosis pathway. Very interestingly, while both PEGylated nanoassemblies kept being uptaken by macrophages, at a significant higher rate than that of cancer cells due to the high phagocytotic activity of the immune cells, significant differentiation operated between M2-like and M1-like macrophages. The former showed enhanced phagocytosis toward nanoassemblies with a less compact PEGylated coating, which opens new routes to perform differentiated treatment with immunomodulatory molecules of pro-inflammatory and immunosuppressive M2-like macrophages, actively participating in tumor growth. Finally, the exposure of the PEGylated nanoassemblies to multicellular tumor spheroids, serving as mimics of solid tumors, conducted to the very slow diffusion of nanoassemblies, whatever their external coating, despite their ability to spontaneously and progressively disassemble in cells, which adverts on the necessary use of appropriate models to assess the efficacy of nanomedicines. Overall, these pioneering studies open the perspectives of time-saving construction of nanoparticles by considering the impact of small hydrophobic units

issued from the incorporation of RAFT CTAs. Depending on their capability to self-assemble and tightly interact with the surface of nano-objects, activating hydrophobic groups of RAFT CTAs can offer control of the compacity of outer hydrophilic shells and rearrangement thereof, following cellular engulfment. Simultaneous exploration of the role of chemical inhibitors and investigations of the rheological properties of the nanoassemblies and their interactions with the serum proteins through fluorescence correlation spectroscopy are under way to understand the mechanical response and cell uptake dynamics of the nanoassemblies with respect to their coating shell.

Author Contributions

TB, JP, CL, JB, CB: Investigation and methodology; EAV, SN, PH, CH, LL, RNM: Formal analyses

EAV, SL: Writing – review & editing

EI and CB: Conceptualization, data curation, formal analysis, funding acquisition and writing - original draft.

Conflicts of interest

There are no conflicts to declare.

Acknowledgements

The authors thank the BIBS platform of Angers-Nantes INRAe center for their kind access to TEM imaging, the cytocell core facility for the flow cytometry experiments, the MicroPICell core facility for microscopy analyses and immuno-histology, the clinical transfer platform (CIC-biothérapies Nantes) for monocyte purification, Manon Besançon for **P3** synthesis, and L. Lartigue for participating in some discussions. TEM data were obtained with the assistance of the IBiSA Electron Microscopy Facility of Tours University. The University of Nantes (Interdisciplinary programs), INSERM, and CNRS through its Mission for Interdisciplinary (Nano Challenge / "Health and well-fare" – ETHICAM project), Région Pays de la Loire (Paris Scientifiques program) and ARSMeso44 are gratefully acknowledged for their strong support. Manon Besançon is The French Ministry of Foreign Affairs and French Embassy in Belgium are strongly acknowledged for their constant support through the Tournesol PHC program despite the current situation. The authors also thank the cluster LUNG innOvatiOn (LUNG^{O2}) for logistic support. This cluster is supported by the National Research Agency under the Programme d'Investissements d'Avenir (ANR-16-IDEX-0007), the Pays de la Loire Region research program and the Institut de Recherche en Santé Respiratoire des Pays de la Loire.

Notes and references

1 A. Sangtani, O. K. Nag, L. D. Field, J. C. Breger and J. B. Delehanty, In *WIREs Nanomed. Nanobiotechnol.*, John Wiley & Sons, Inc.: 2017; p e1466. doi: 1410.1002/wnan.1466.

2 J. V. Jokerst and S. S. Gambhir, *Acc. Chem. Res.*, 2011, **44**, 1050-1060.

3 S. Kunjachan, J. Ehling, G. Storm, F. Kiessling and T. Lammers, *Chem. Rev.*, 2015, **115**, 10907-10937.

4 G. Chen, I. Roy, C. Yang and P. N. Prasad, *Chem. Rev.*, 2016, **116**, 2826-2885. View Article Online DOI: 10.1039/D1NR06769A

5 J. A. Barreto, W. O'Malley, M. Kubeil, B. Graham, H. Stephan and L. Spiccia, *Adv. Mater.*, 2011, **23**, H18-H40.

6 S. Zhang, H. Gao and G. Bao, *ACS Nano*, 2015, **9**, 8655-8671.

7 K. Zarschler, L. Rocks, N. Licciardello, L. Boselli, E. Polo, K. P. Garcia, L. De Cola, H. Stephan and K. A. Dawson, *Nanomed.: Nanotechnol. Biol. Med.*, 2016, **12**, 1663-1701.

8 S. Dasgupta, T. Auth and G. Gompper, *Nano Lett.*, 2014, **14**, 687-693.

9 A. Albanese, P. S. Tang and W. C. W. Chan, *Annu. Rev. Biomed. Eng.*, 2012, **14**, 1-16.

10 Y. Li, M. Kroger and W. K. Liu, *Nanoscale*, 2015, **7**, 16631-16646.

11 A. Verma and F. Stellacci, *Small*, 2010, **6**, 12-21.

12 A. C. Anselmo, M. W. Zhang, S. Kumar, D. R. Vogus, S. Menegatti, M. E. Helgeson and S. Mitragotri, *ACS Nano*, 2015, **9**, 3169-3177.

13 A. C. Anselmo and S. Mitragotri, *Adv. Drug Delivery Rev.*, 2017, **108**, 51–67.

14 L. Shang and G. U. Nienhaus, *Acc. Chem. Res.*, 2017, **50**, 387-395.

15 M. I. Setyawati, C. Y. Tay, D. Docter, R. H. Stauber and D. T. Leong, *Chem. Soc. Rev.*, 2015, **44**.

16 A. S. Karakoti, S. Das, S. Thevuthasan and S. Seal, *Angew. Chem. Int. Ed.*, 2011, **50**, 1980-1994.

17 J. V. Jokerst, T. Lobovkina, R. N. Zare and S. S. Gambhir, *Nanomedicine (Lond)*, 2011, **6**, 715-728.

18 H.-S. Han, J. D. Martin, J. Lee, D. K. Harris, D. Fukumura, R. K. Jain and M. Bawendi, *Angew. Chem. Int. Ed.*, 2013, **52**, 1414-1419.

19 A. B. Lowe and C. L. McCormick, *Chem. Rev.*, 2002, **102**, 4177-4190.

20 L. Ye, Y. B. Zhan, B. G. Yang, X. Zhou, J. J. Li, Z. H. Qin, D. Y. Dong, Y. L. Cui and F. L. Yao, *ACS Appl. Mater. Interfaces*, 2016, **8**, 4385-4398.

21 M. Uz, V. Bulmus and S. A. Altinkaya, *Langmuir*, 2016, **32**, 5997-6009.

22 H. Zhou, Z. Y. Fan, P. Y. Li, J. J. Deng, D. C. Arhontoulis, C. Y. Li, W. B. Bowne and H. Cheng, *ACS Nano*, 2018, **12**, 10130-10141.

23 C. Yang, S. Gao, F. Dagnæs-Hansen, M. Jakobsen and J. Kjems, *ACS Appl. Mater. Interfaces*, 2017, **9**, 12203-12216.

24 J. Suk, Q. Xu, N. Kim, J. Hanes and L. Ensign, *Adv. Drug. Deliv. Rev.*, 2016, **99**, 28-51.

25 B. Pelaz, P. del Pino, P. Maffre, R. Hartmann, M. Gallego, S. Rivera-Fernandez, J. M. de la Fuente, G. U. Nienhaus and W. J. Parak, *ACS Nano*, 2015, **9**, 6996-7008.

26 R. Huang, R. P. Carney, K. Ikuma, F. Stellacci and B. L. T. Lau, *ACS Nano*, 2014, **8**, 5402-5412.

27 K. Saha, M. Rahimi, M. Yazdani, S. T. Kim, D. F. Moyano, S. Hou, R. Das, R. Mout, F. Rezaee, M. Mahmoudi and V. M. Rotello, *ACS Nano*, 2016, **10**, 4421-4430.

28 S. Sengupta and A. Kulkarni, *ACS Nano*, 2013, **7**, 2878-2882.

29 C. Cruje and D. Chithrani, *J. Nanomed. Res.*, 2014, **1**, 00006.

30 C. Pereira Gomes, V. Leiro, C. D. Ferreira Lopes, A. P. Spencer and A. P. Pêgo, *Acta Biomater.*, 2018, **78**, 247-259.

31 D. F. Liu, W. Wu, J. J. Ling, S. Wen, N. Gu and X. Z. Zhang, *Adv. Func. Mater.*, 2011, **21**, 1498-1504.

32 E. Poselt, H. Kloust, U. Tromsdorf, M. Janschel, C. Hahn, C. Masslo and H. Weller, *ACS Nano*, 2012, **6**, 1619-1624.

33 N. J. J. Johnson, S. He, V. A. N. Hun and A. Almutairi, *ACS Nano*, 2016, **10**, 8299-8307.

34 W. Braunecker and K. Matyjaszewski, *Prog. Polym. Sci.*, 2007, **32**, 93–146.

35 C. Boyer, V. Bulmus, T. P. Davis, V. Ladmiral, J. Liu and S. Perrier, *Chem. Rev.*, 2009, **109**, 5402-5436.

36 A. Favier and M.-T. Charreyre, *Macromol. Rapid Commun.*, 2006, **27**, 653-692.
37 L. K. Müller, J. Simon, C. Rosenauer, V. Mailänder, S. Morsbach and K. Landfester, *Biomacromolecules*, 2018, **19**, 374-385.
38 C. Weber, S. Morsbach and K. Landfester, *Angew. Chem. Int. Ed.*, 2019, **58**, 12787-12794.
39 C. Linot, J. Poly, J. Boucard, D. Pouliquen, S. Nedellec, P. Hulin, N. Marec, P. Arosio, A. Lascialfari, A. Guerrini, C. Sangregorio, M. Lecouvey, L. Lartigue, C. Blanquart and E. Ishow, *ACS Appl. Mater. Interfaces*, 2017, **9**, 14242-14257.
40 K. Binnemars-Postma, G. Storm and J. Prakash, *Int. J. Mol. Sci.*, 2017, **18**.
41 S. Klebe, J. Leigh, D. W. Henderson and M. Nurminen, *Int. J. Environ. Res. Public Health*, 2020, **17**.
42 N. van Zandwijk, G. Reid and A. L. Frank, *Expert Rev. Anticancer Ther.*, 2020, **20**, 271-278.
43 N. C. Bigall, W. J. Parak and D. Dorfs, *Nano Today*, 2012, **7**, 282-296.
44 A. Faucon, T. Maldiney, O. Clément, P. Hulin, S. Nedellec, M. Robard, N. Gautier, E. De Meulenaere, K. Clays, T. Orlando, A. Lascialfari, C. Fiorini-Debuisschert, J. Fresnais and E. Ishow, *J. Mater. Chem. B*, 2014, **2**, 7747-7755.
45 N. M. Pinkerton, M. E. Gindy, V. L. Calero-DdelC, T. Wolfson, R. F. Pagels, D. Adler, D. Y. Gao, S. K. Li, R. B. Wang, M. Zevon, N. Yao, C. Pacheco, M. J. Therien, C. Rinaldi, P. J. Sinko and R. K. Prud'homme, *Adv. Healthcare Mater.*, 2015, **4**, 1376-1385.
46 C. Kaewsaneha, P. Tangboriboonrat, D. Polpanich and A. Elaissari, *ACS Appl. Mater. Interfaces*, 2015, **7**, 23373-23386.
47 C. Monzel, C. Vicario, J. Piehler, M. Coppey and M. Dahan, *Chem. Sci.*, 2017, **8**, 7330-7338.
48 O. Chen, L. Riedemann, F. Etoc, H. Herrmann, M. Coppey, M. Barch, C. T. Farrar, J. Zhao, O. T. Bruns, H. Wei, P. Guo, J. Cui, R. Jensen, Y. Chen, D. K. Harris, J. M. Cordero, Z. W. Wang, A. Jasanoff, D. Fukumura, R. Reimer, M. Dahan, R. K. Jain and M. G. Bawendi, *Nat. Commun.*, 2014, **5**, 5093.
49 E. Teston, Y. Lalatonne, D. Elgrabli, G. Autret, L. Motte, F. Gazeau, D. Scherman, O. Clement, C. Richard and T. Maldiney, *Small*, 2015, **11**, 2696-2704.
50 M. Mahmoudi, H. Hofmann, B. Rothen-Rutishauser and A. Petri-Fink, *Chem. Rev.*, 2011, **112**, 2323-2338.
51 S. Laurent, D. Forge, M. Port, A. Roch, C. Robic, L. Vander Elst and R. N. Muller, *Chem. Rev.*, 2008, **108**, 2064-2110.
52 L. H. Reddy, J. L. Arias, J. Nicolas and P. Couvreur, *Chem. Rev.*, 2012, **112**, 5818-5878.
53 A. Faucon, H. Benhelli-Mokrani, F. Fleury, S. Dutertre, M. Tramier, J. Boucard, L. Lartigue, S. Nedellec, P. Hulin and E. Ishow, *Nanoscale*, 2017, **9**, 18094–18106.
54 A. Faucon, H. Benhelli-Mokran, F. Fleury, L. Dubreil, P. Hulin, S. Nedellec, T. Doussineau, R. Antoine, T. Orlando, A. Lascialfari, J. Fresnais, L. Lartigue and E. Ishow, *J. Colloid Interface Sci.*, 2016, **479**, 139–149.
55 A. Faucon, R. Lenk, J. Hemez, E. Gautron, D. Jacquemin, J.-Y. Le Questel, J. Graton, A. Brosseau and E. Ishow, *Phys. Chem. Chem. Phys.*, 2013, **15**, 12748-12756.
56 A. Faucon, J. Fresnais, A. Brosseau, P. Hulin, S. Nedellec, J. Hemez and E. Ishow, *J. Mater. Chem. C*, 2013, **1**, 3879-3886.
57 V. Torrisi, A. Graillot, L. Vitorazi, Q. Crouzet, G. Marletta, C. Loubat and J. F. Berret, *Biomacromolecules*, 2014, **15**, 3171-3179.
58 A. K. Varkouhi, M. Scholte, G. Storm and H. J. Haisma, *J. Control. Release*, 2011, **151**, 220-228.
59 J. Boucard, C. Linot, T. Blondy, S. Nedellec, P. Hulin, C. Blanquart, L. Lartigue and E. Ishow, *Small*, 2018, **14**, 1802307.
60 B. Zhao, G. Z., M. Johnson, E. Najafidehaghani, T. Rejek, A. George, R. H. Fink, A. Turchanin and M. Halik, *Adv. Funct. Mater.*, 2021, **31**, 2105444.
61 C. Henoumont, S. Laurent, R. N. Muller and L. Vander Elst, *Anal. Chem.*, 2015, **87**, 1701-1710.
62 E. Mansfield, K. M. Tyner, C. M. Poling and J. L. Blacklock, *Anal. Chem.*, 2014, **86**, 1478-1484.
63 N. T. Huynh, E. Roger, N. Lautram, J. P. Benoit and C. Passirani, *Nanomedicine (Lond)*, 2010, **5**, 1415-1433.
64 Y. Matsumura and H. Maeda, *Cancer Res.*, 1986, **46**, 6387-6392.
65 V. Francia, D. Montizaan and A. Salvati, *Beilstein J Nanotechnol.*, 2020, **11**, 338-353.
66 L. W. C. Ho, W. Y. Yung, K. H. S. Sy, H. Y. Li, C. K. K. Choi, K. C. F. Leung, T. W. Y. Lee and C. H. J. Choi, *ACS Nano*, 2017, **11**, 6085-6101.
67 Y. Li, M. Kroger and W. K. Liu, *Biomaterials*, 2014, **35**, 8467-8478.
68 A. K. Pearce and R. K. O'Reilly, *Biomacromolecules*, 2021, **22**, 4459-4469.
69 L. Martin, R. Peltier, A. Kuroki, J. S. Town and S. Perrier, *Biomacromolecules*, 2018, **19**, 3190-3200.
70 J. J. Rennick, A. P. R. Johnston and R. G. Parton, *Nature Nanotech.*, 2021, **16**, 266-276.
71 S. D. Conner and S. L. Schmid, *Nature*, 2003, **422**, 37-44.
72 M. S. de Almeida, E. Susnik, B. Drasler, P. Taladriz-Blanco, A. Petri-Fink and B. Rothen-Rutishauser, *Chem. Soc. Rev.*, 2021, **50**, 5397-5434.
73 A. Faucon, H. Benhelli-Mokrani, L. A. Córdova, B. Brulin, D. Heymann, P. Hulin, S. Nedellec and E. Ishow, *Adv. Healthcare Mater.*, 2015, **4**, 2727-2734.
74 M. Breton, G. Prevel, J. F. Audibert, R. Pansu, P. Tauc, B. Le Pioufle, O. Francais, J. Fresnais, J. F. Berret and E. Ishow, *Phys. Chem. Chem. Phys.*, 2011, **13**, 13268-13276.
75 C. Wong, T. Stylianopoulos, J. A. Cui, J. Martin, V. P. Chauhan, W. Jiang, Z. Popovic, R. K. Jain, M. G. Bawendi and D. Fukumura, *Proc. Natl. Acad. Sci. USA*, 2011, **108**, 2426-2431.
76 S. Gordon and A. Pluddemann, *BMC Biology*, 2017, **15**.
77 J. Zhou, Z. Tang, S. Gao, C. Li, Y. Feng and X. Zhou, *Front Oncol.*, 2020, **10**, 188.
78 P. Italiani and D. Boraschi, *Front. Immun.*, 2014, **5**.
79 A. Mantovani, F. Marchesi, A. Malesci, L. Laghi and P. Allavena, *Nat. Rev. Clin. Oncol.* , 2017, **14**, 399–416.
80 M. Schroffenegger, N. S. Leitner, G. Morgese, S. N. Ramakrishna, M. Willinger, E. M. Benetti and E. Reimhult, *ACS Nano*, 2020, **14**, 12708-12718.
81 M. Y. Li, S. Jiang, J. Simon, D. Passlick, M. L. Frey, M. Wagner, V. Mailander, D. Crespy and K. Landfester, *Nano Letters*, 2021, **21**, 1591-1598.
82 V. Murthy, D. Katzman and D. H. Sterman, *Clin. Respir. J.*, 2019, **13**, 272-279.
83 S. Biffi, R. Voltan, B. Bortot, G. Zauli and P. Secchiero, *Expert Opin. Drug. Deliv.*, 2019, **16**, 481–496.
84 S. Lim, J. Park, M. K. Shim, W. Um, H. Y. Yoon, J. H. Ryu, D.-K. Lim and K. Kim, *Theranostics*, 2019, **9**, 7906-7923.
85 F. Gueugnon, S. Leclercq, C. Blanquart, C. Sagan, L. Cellerin, M. Padieu, C. Perigaud, A. Scherpereel and M. Gregoire, *Am. J. Pathol.*, 2011, **178**, 1033-1042.
86 A.-L. Chéné, S. d'Almeida, T. Blondy, J. Tabiasco, S. Deshayes, J.-F. Fonteneau, L. Cellerin, Y. Delneste, M. Grégoire and C. Blanquart, *J.Thorac. Oncol.*, 2016, **11**, 1765-1773.